Induced charges in a Thomas–Fermi metal: insights from molecular simulations

Swetha Nair, Giovanni Pireddu, Benjamin Rotenberg

Induced charges in a Thomas-Fermi metal:
insights from molecular simulations

Swetha Nair,[1] Giovanni Pireddu,[1] and Benjamin Rotenberg[1,2,*]

[1]*Sorbonne Université, CNRS, Physicochimie des électrolytes et nanosystèmes interfaciaux,*
UMR 8234 PHENIX, F-75005, Paris, France
[2]*Réseau sur le Stockage Electrochimique de l'Energie (RS2E),*
FR CNRS 3459, 80039 Amiens Cedex, France

Abstract

We study the charge induced in a Thomas-Fermi metal by an ion in vacuum, using an atomistic description employed in constant-potential molecular dynamics simulations, and compare the results with the predictions from continuum electrostatics. Specifically, we investigate the effects of the Thomas-Fermi screening length l_{TF} and the position d of the ion with respect to the surface on the induced charge distribution in a graphite electrode. The continuum predictions capture most of the features observed with the atomistic description (except the oscillations due to the atomic sites of the graphite lattice), provided that d and l_{TF} are larger than the inter-atomic distances within the electrode. At large radial distance from the ion, the finite l_{TF} case can be well approximated by the solution for a perfect metal using an effective distance $d+l_{TF}$. This requires a careful definition of the effective interface between the metal and vacuum for the continuum description. Our atomistic results support in particular an early analytical prediction [Vorotyntsev and Kornyshev, *Sov. Phys. JETP* **51**, 509 (1980)] for a single charge at the interface between a Thomas-Fermi metal and a polarizable medium, which remains to be tested in atomistic simulations with an explicit solvent.

---

[*] benjamin.rotenberg@sorbonne-universite.fr

I. INTRODUCTION

The polarization of a metallic surface by an electrolyte solution, which plays a key role in electrochemistry or for the electrochemical storage of energy, results from the interplay of the charge distributions on both sides of the interface. Firstly, a polar solvent screens the electrostatic interactions between ions, which in a continuum picture is simply reduced by a factor equal to the solvent relative permittivity ϵ_r. The distance over which this screened interaction between two elementary charges e is equal to the thermal energy, is the so-called Bjerrum length $l_B = e^2/4\pi\epsilon_0\epsilon_r k_B T$, with ϵ_0 the vacuum permittivity, k_B Boltzmann's constant and T the temperature ($l_B \approx 7$ Å in water at room temperature). Secondly, the combined effect of thermal motion and electrostatic interactions between ions results in ionic screening. In dilute electrolytes, Debye-Hückel theory predicts that the characteristic length for the decay of electrostatic interactions is the Debye screening length, which depends on the Bjerrum length, as well as the concentrations and the valencies of the ions. Finally, in metals the screening of the electric field by electrons can be described *e.g.* by Lindhardt theory, which reduces in the long-wavelength limit to the Thomas-Fermi model of screening [1, 2]. The characteristic length for the decay inside the metal is the Thomas-Fermi screening length, l_{TF}, which depends on the density of states at the Fermi level [3].

Screening inside the metal has important consequences on the charge induced by an external charge distribution, on electrostatic interactions between ions near the surface and in turn on the structure of the electric double layer, on the capacitance of the interface and more generally on interfacial thermodynamics and kinetics. These aspects have been successfully investigated in the framework of continuum (in particular non-local) electrostatics [4–14]. In particular, Kornyshev and co-workers showed that the potential arising from a point charge at the interface between a dielectric medium (with permittivity ϵ_1) and Thomas-Fermi metal (with dielectric function $\epsilon(k) = \epsilon_2 \times (1 + k_{TF}^2/k^2)$, where $k_{TF} = l_{TF}^{-1}$ is the reciprocal of the Thomas-Fermi screening length and k the wavevector) decays laterally with a characteristic length $\propto \epsilon_1 l_{TF}/\epsilon_2$, *i.e.* involving the properties of both materials. In parallel, the response of the electronic distribution of metals has been analyzed using electronic Density Functional Theory (DFT), initially explored in 1D geometries [15–17], with subsequent studies incorporating more advanced functionals and atomically resolved surfaces [18, 19], particularly within the framework of the Jellium (uniform electron gas) model. In order to link such

descriptions with the continuum picture, one needs in particular to address the question of where to locate the interface, so-called "Jellium edge", between the metal and the external medium (vacuum or liquid).

From the simulation point of view, efficient algorithms have also been introduced to capture the mutual polarization of media with different permittivities in the presence of ions, to investigate the properties of interfacial electrolytes described by explicit ions in an implicit solvent [20–27]. *Ab initio* [28–34] and classical [35–47] molecular dynamics simulations have also become an essential tool to investigate electrode/electrolyte interfaces and electrochemical systems taking into account the atomic structure of the metal and the molecular features of the electrolyte. The charge induced inside the metal by the electrolyte plays a role on the interfacial structure, dynamics and thermodynamics [48–57]; the statistics of its fluctuations can further be used as a powerful probe of the latter [58–61]. Some strategies have also been introduced to describe Thomas-Fermi metals in such molecular simulations, which are able to capture screening within the metal and its consequences on interfacial thermodynamics [62–64]. The metallicity of the electrode, which reflects its electronic structure, affects the electron transfer kinetics. Recent experiments showed that the kinetics of a heterogeneous electron transfer reaction at well-defined twisted bilayer graphene (TBG) surfaces can be tuned by the interlayer Moiré twist angle between the two layers [65]. Even more recently, molecular simulations and continuum dielectric theory further analyzed the origin of these observations, linking the twist angle to the Thomas-Fermi screening length via the density of states (DOS) of the TBG [66]. The connection between DOS and Thomas-Fermi screening length was also explored in the context of classical molecular simulations [67], specifically with the width of the Gaussian distribution describing the charge density around electrode atoms in fluctuating charge models (see Section II B).

Recently, we investigated the charge induced in a perfect metal ($l_{TF} = 0$) by a single ion near a model gold electrode using classical molecular simulations in the constant-potential ensemble, focusing on the effects of the atomic lattice of the solid and of a molecular solvent (water), compared to an ion in vacuum and with analytical predictions from continuum electrostatics [68]. In the present work, we consider instead the effects of screening inside the solid (tuned via the Thomas-Fermi length l_{TF}) on the charge induced by an ion in vacuum. We address in particular the effects of periodic boundary conditions employed in simulations, for the comparison of our atomistic results with analytical theories. We analyse

the induced charge distribution both in real and reciprocal space to quantify its lateral decay as a function of the Thomas-Fermi length and the distance of the ion from the first atomic plane of the electrode. We finally discuss how to bridge the atomistic and continuum pictures, which requires identifying the location of an effective sharp interface between the metal and vacuum. Section II introduces the considered system and its description by continuum electrostatics and atomistic simulations, while Section III presents the results and discussion.

II.   SYSTEM AND METHODS

A.   Theory

In the continuum picture, the charge induced in a Thomas-Fermi metal, characterized by a permittivity ϵ_2 and a Thomas-Fermi screening length l_{TF}, by a point charge q_{ion} in a polarizable medium characterized by a permittivity ϵ_1 at a distance d from the interface (see Fig. 1c) can be computed from the electrostatic potential $\psi(\mathbf{r})$. The latter satisfies $\Delta\psi_2 = k_{TF}^2\psi_2$ inside the metal (defined here by the region $z < 0$), with $k_{TF} = l_{TF}^{-1}$ the Thomas-Fermi wavevector, and $\Delta\psi_1 = -\rho_{el}/\epsilon_0\epsilon_1$ outside ($z > 0$), where $\rho_{el}(\mathbf{r}) = q_{ion}\delta(\mathbf{r}-\mathbf{r}_{ion})$ is the volumic charge density and ϵ_0 the vacuum permittivity, together with the continuity of the potential and of the electric displacement $-\epsilon\partial_z\psi$ at the interface. The solution to this problem can be found explicitly *e.g.* in Ref. [14], using cylindrical coordinates (with r the radial distance from the ion) and the Hankel transform of the observables such as the potential $f(z, k) = \int_0^\infty f(z, r)J_0(kr)r\mathrm{d}r$, with J_0 the zeroth order Bessel function of the first kind. The volumic induced charge density can then be computed as $\rho_{ind}^{3D}(z, k) = -\epsilon_0\epsilon_2 k_{TF}^2\psi_2(z, k)$, with the result:

$$\rho_{ind}^{3D}(z, k) = \frac{-\epsilon_2 k_{\mathrm{TF}}^2 q_{ion}e^{-kd+\sqrt{k^2+k_{\mathrm{TF}}^2}z}}{2\pi(\epsilon_1 k + \epsilon_2\sqrt{k^2 + k_{\mathrm{TF}}^2})} \ . \tag{1}$$

The inverse Hankel transform is not known analytically for finite l_{TF}, but this expression shows that the induced charge decays exponentially within the metal, and that the radial distribution depends on the depth. For a perfect metal ($l_{TF} = 0$), the induced charge is localized at the interface ($z = 0$) and the surface density is [69]:

$$\sigma_{ind}^{l_{TF}=0}(r) = -\frac{q_{ion}}{2\pi}\frac{d}{(r^2 + d^2)^{3/2}} \tag{2}$$
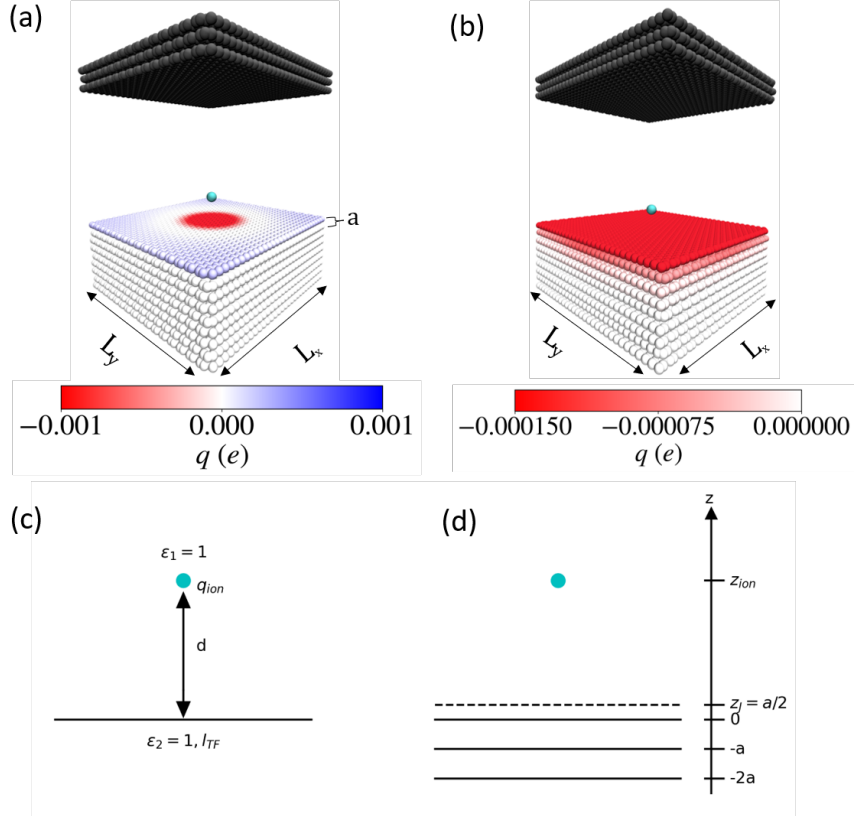
FIG. 1. The system consists of a single ion in vacuum next to a Thomas-Fermi metal. Panels (a) and (b) illustrate the corresponding simulation box, which contains a graphite electrode with explicit atoms (with interplane distance a), an ion (here located at a distance $z_{ion} = 7.8$ Å from the first atomic plane of the electrode, in cyan) and an insulating wall (in black); the color of electrode atoms indicates their charge induced by the ion, for a Thomas-Fermi screening length $l_{TF} = 0$ and 5 Å in panels (a) and (b), respectively. Periodic boundary conditions are used in the x and y directions only. Panel (c) shows the corresponding continuum picture for a single point charge q_{ion} at a distance d from the interface between two media: vacuum (with relative permittivity ϵ_1) and a Thomas-Fermi metal, with a dielectric function $\epsilon(k) = \epsilon_2 \times (1 + k_{TF}^2/k^2)$ with $k_{TF} = l_{TF}^{-1}$ the reciprocal of the Thomas-Fermi screening length, k the wavevector and $\epsilon_2 = 1$. Panel (d) illustrates the issue of defining the location of the interface z_{int} in the continuum picture from the discrete representation and the position z_{ion} of the ion with respect to the first atomic plane; the position of the Jellium edge can be approximated as $z_J = +a/2$, with a the interplane distance.

In the following, we will describe results from molecular simulations, in which periodic boundary conditions (PBC) in the directions parallel to the interface are employed. The

external charge distribution inducing the polarization of the metal does not correspond to a single charge, but rather to a periodic array of charges q_{ion} on a rectangular lattice, with dimensions L_x and L_y. The solution of the corresponding electrostatic problem can be solved explicitly using cartesian coordinates as a sum over modes (see below). For finite l_{TF}, the induced charge also decays exponentially and the distribution in the x and y directions also depends on the depth z within the metal. In order to analyze the effect of l_{TF} on the lateral distribution, it is convenient to introduce the 2D charge density obtained by integrating over the z direction inside the metal:

$$\sigma_{ind}(x,y) = \int_{-\infty}^{0} \rho_{el}(x,y,z)\,\mathrm{d}z \; . \tag{3}$$

The solution for finite l_{TF}, which can be obtained by considering the Fourier coefficients, reads:

$$\sigma_{ind}(x,y) = \frac{-q_{ion}}{L_x L_y} \sum_{m=0}^{\infty} \sum_{n=0}^{\infty} a_{m,n} \frac{\epsilon_2 k_{TF}^2 e^{-k_{m,n}d} \cos(k_m x)\cos(k_n y)}{\sqrt{k_{m,n}^2 + k_{TF}^2}(\epsilon_1 k_{m,n} + \epsilon_2 \sqrt{k_{m,n}^2 + k_{TF}^2})} \tag{4}$$

where we have introduced the wavevectors $k_m = m \times (2\pi/L_x)$, $k_n = n \times (2\pi/L_y)$ and $k_{m,n} = \sqrt{k_m^2 + k_n^2}$ as well as the weights $a_{0,0} = 1$, $a_{m,0} = a_{0,n} = 2$ and $a_{m,n} = 4$. While this result shares obvious similarities with the single charge case (see Eq. 1 above for the 3D density, and Eq. 17 of Ref. [14] for the 2D density), to the best of our knowledge the solution under PBC has not been reported previously. The terms in Eq. 4 decay exponentially fast with ion-surface distance, except for $k_{m,n} = 0$, which corresponds to a uniform surface charge density $-q_{ion}/L_x L_y$. As a result, when $d \gg L_x, L_y$ so that $k_{m,n}d \gg 1$, one recovers the result for a parallel plate capacitor (one side being the periodic array of ions, the other the metallic electrode bearing the image charge). For comparison with the solution for a perfect metal Eq. 2, we will also compute the radial distribution:

$$\sigma_{ind}(r) = \frac{1}{2\pi r} \iint \sigma_{ind}(x,y)\delta\left(r - \sqrt{x^2 + y^2}\right)\,\mathrm{d}x\mathrm{d}y \; , \tag{5}$$

with δ Dirac's Delta function as well as its running integral:

$$Q_{ind}(r) = \int_0^r \sigma_{ind}(r')2\pi r'\,\mathrm{d}r' \; . \tag{6}$$

Only $r < \min\{L_x, L_y\}/2$ is considered in the periodic case. In the present work, we consider the case of an interface between a Thomas-Fermi metal and vacuum, which corresponds to $\epsilon_1 = \epsilon_2 = 1$.

B. Simulation

1. Thomas-Fermi model

For an atomistic description of the metal polarization by an external charge, we use the constant-potential, fluctuating-charge model introduced by Siepmann and Sprik for the classical molecular simulation of water/electrode interfaces [35], later applied to electrochemical cells [70] and recently extended to take the Thomas-Fermi length into account [62, 64]. In this model, each electrode atom i at position $\mathbf{r}_i$ with charge q_i contributes to the total charge density as

$$\rho_{elec}(\mathbf{r}) = \sum_{i \in elec} \frac{q_i}{(2\pi w^2)^{3/2}} e^{-|\mathbf{r} - \mathbf{r}_i|^2/2w^2} \ , \tag{7}$$

where w is a fixed width of the Gaussian distribution around each atom. The instantaneous charges of all electrode atoms depend on the external charge distribution, $i.e.$ the positions $\mathbf{r}^N$ of atoms in the electrolyte (in the present study a single ion in vacuum). Specifically, they are determined by the constraints of constant potential imposed on each atom (one common value for all atom in a given electrode) and of global electroneutrality of the system [46, 60]. This process to compute the set of electrode charges $\mathbf{q} = \{q_i\}_{i \in elec}$ involves the potential energy of the system, which owing to the form of electrostatic interactions can be written as:

$$U(\mathbf{r}^N, \mathbf{q}) = \frac{\mathbf{q}^T \mathbf{A} \mathbf{q}}{2} - \mathbf{q}^T \mathbf{B}(\mathbf{r}^N) + C(\mathbf{r}^N) \ , \tag{8}$$

where the first term accounts for electrostatic interactions between electrode atoms, the second for those between electrode and electrolyte, and the third for all other interactions. The scalar C is independent of electrode charges $\mathbf{q}$. Both the matrix $\mathbf{A}$ and vector $\mathbf{B}$ take into account Gaussian nature of the charge distribution of electrode atoms and the PBC inherent in molecular simulations of condensed matter systems. While this description was initially introduced for perfect metals, Scalfi $et\ al.$ extended it to the Thomas-Fermi model, by including the kinetic energy of the free electron gas as in the original Thomas-Fermi approach. By making further approximations to the description of the local density in the fluctuating charge approach, they showed that the Thomas-Fermi model can be recast in the same form simply by introducing an additional term in the matrix describing electrode-

electrode interactions, namely [62]:

$$\mathbf{A}(l_{TF}) = \mathbf{A_0} + \frac{l_{TF}^2 \bar{\rho}_{at}}{\epsilon_0}\mathbf{I} \, , \tag{9}$$

where $\mathbf{A_0}$ is the matrix for $l_{TF} = 0$, $\bar{\rho}_{at}$ is the atomic density of the electrode and $\mathbf{I}$ is the identity matrix. This description, already implemented in several simulation packages [71–73] allows to tune the metallic character of the metal without additional computational cost.

2. Simulation details

Specifically, we consider a system consisting of a graphite electrode, a single Na$^+$ ion in vacuum (with charge $q_{ion} = +e$, with e the elementary charge), and an insulating neutral surface (which doesn't play a role in the present solvent-free case). This is illustrated in Figure 1(a) and (b), with the color indicating the charge of each electrode atom for $l_{TF} = 0$ and 5 Å, respectively. The graphite electrode, maintained at a fixed potential (whose value is irrelevant since there is no counter-electrode), consists of 17280 atoms in an hexagonal lattice arranged in 9 atomic planes perpendicular to the z direction. The distance between carbon atoms within a plane is $d_{CC} = 1.42$ Å, while the distance between planes is $a = 3.354$ Å. The width of the Gaussian distribution around each atom $w = 0.4$ Å, and the Thomas-Fermi length l_{TF} ranges from 0 Å to 5 Å. Even for the largest l_{TF} considered, the electrode is sufficiently thick to ensure that the charges on the last atomic planes are negligible. The insulating wall consists of 5760 carbon atoms arranged in 3 planes with the same graphite structure. The atomic plane closest to the ion is located at $z = 0$ for the metal, while that of the insulating wall is at $z = 55.088$ Å. In order to investigate the effect of the ion-electrode distance on the induced charge distribution, we consider positions $z_{ion} = 5.1, 7.8, 11.0$ and 15.0 Å. These values were chosen based on the equilibrium density profile of Na$^+$ at the interface between graphite and a 1 M NaCl aqueous solution using the same model (see Appendix). The box dimensions are $L_x = 68.20$ Å, $L_y = 73.83$ Å and $L_z = 231.79$ Å, and PBC are applied only in the x and y directions.

Electrostatic interactions are computed by 2D Ewald summation, taking into account the Gaussian distributions of electrode atoms and the point charge of the ion [72]. Even though they do not play a role in the present calculation, we also introduce non-electrostatic inter-

8

actions via truncated and shifted Lennard-Jones (LJ) potentials, using the LJ parameters for Na^+ and carbon from Refs. [74] and [75], respectively, with Lorentz-Berthelot mixing rules. All simulations are performed using the molecular dynamics code Metalwalls [71], and the charges on the electrode atoms are determined using matrix inversion [60]. Since there is no solvent and the ion is fixed, a single simulation step is sufficient to determine the induced charge on each atom. The 3D charge density can then be reconstructed with Eq. 7 and integrated as indicated in Eq. 3 to obtain the 2D charge density. In practice, it is more efficient to perform the integration over z analytically and simply reconstruct the 2D distribution directly as

$$\sigma_{ind}^{MD}(x,y) = \sum_{i\in elec} \frac{q_i}{2\pi w^2} e^{-[(x-x_i)^2+(y-y_i)^2]/2w^2} . \tag{10}$$

This quantity is computed on a 2D grid with bin width $h = 0.1$ Å, where the charge in each bin is computed using the analytical integral of the 2D Gaussian distributions. Explicitly, $\sigma_{ind}^{MD}(x,y)h^2 = \sum_{i\in elec} q_i I(x,x_i) I(y,y_i)$, with $I(x,x_i) = \frac{1}{2}\left(\mathrm{erf}\left[(x+h/2-x_i)/w\right] - \mathrm{erf}\left[(x-h/2-x_i)/w\right]\right)$, where erf is the error function. The radial distribution can then be obtained numerically by Eq. 5.

III. RESULTS AND DISCUSSION

In the following, we present the results for the charge induced on the electrode obtained with the atomistic description, compare them with various analytical predictions within the continuum picture and discuss in particular the links between the two levels of description. The snapshots introducing the system in Fig. 1 illustrate the main effects of introducing a finite Thomas-Fermi screening length. While for a perfect metal ($l_{TF} = 0$ Å, panel 1a) the charge is essentially localized in the first atomic plane of the electrode and decays away from the atom, for $l_{TF} = 5$ Å a significant charge is induced on at least one more atomic plane and the lateral distribution visible in the first plane is much more homogeneous. The exponential decay of the charge per plane within the electrode (with a characteristic length l_{TF}) was demonstrated for capacitors with vacuum or an electrolyte solution between two electrodes in Ref. [62] introducing the Thomas-Fermi model in constant-potential, fluctuating charge simulations. Here we focus on the lateral distribution of the induced charge, by considering the integrated charge density $\sigma_{ind}(x,y)$ defined by Eq. 3. We begin with a qualitative analysis

of 2D maps of the induced charge in Section III A, before turning to a quantitative analysis of the radial charge distribution in Section III B and of the 2D distribution in reciprocal space in Section III C.

A. Qualitative analysis with 2D maps of the induced charge

1. *Effect of ion-surface distance for a perfect metal*

We start by briefly recalling the effect of an ion-surface distance for the case of a perfect metal ($l_{TF} = 0$), already investigated in Ref. [68] for a gold electrode (FCC lattice structure) and a slightly different setup including a countercharge on the insulating wall (resulting with the ion in a net zero charge induced on the electrode). Fig. 2 shows the surface charge density $\sigma_{ind}(x, y)$ induced in the graphite electrode, described as a perfect metal ($l_{TF} = 0$ Å), by a Na$^+$ ion located at $(x, y) = (0, 0)$ and a distance from the first atomic plane of the electrode $z_{ion} = 5.1, 7.8$ and 11 Å for panels (a), (b) and (c), respectively.

Despite an obvious difference, namely the spatial variations associated with the discrete atomic structure of the electrode (modulated by the Gaussian distribution around each atom, see also Section III C), the results are overall consistent with the continuum picture. For each distance of the Na$^+$ ion from the surface, the induced charge is more negative close to the ion and decays away from it, consistently with Eq. 2. The slightly positively charged regions (blue) correspond to atoms in the second atomic plane of the electrode and likely results from the nearby large negative charges, as already observed in Ref. [68]. Increasing the distance of the ion from the surface results in a less negative charge density close to the ion and in a slower lateral decay, consistently with Eq. 2, and in a more homogeneous charge distribution (see also Section III B 1).

2. *Effect of the Thomas-Fermi screening length*

We now turn to the effect of the Thomas-Fermi screening length on the charge distribution induced by the ion, which had not been considered previously. Fig. 3 shows the surface charge density $\sigma_{ind}(x, y)$ for an ion located at $(x, y) = (0, 0)$ and a distance $z_{ion} = 5.1$ Å from the first atomic plane of the electrode, for $l_{TF} = 0, 3$ and 5 Å in panels (a), (b) and (c), respectively (panel 3a is therefore identical to panel 2a). Consistently with the continuum
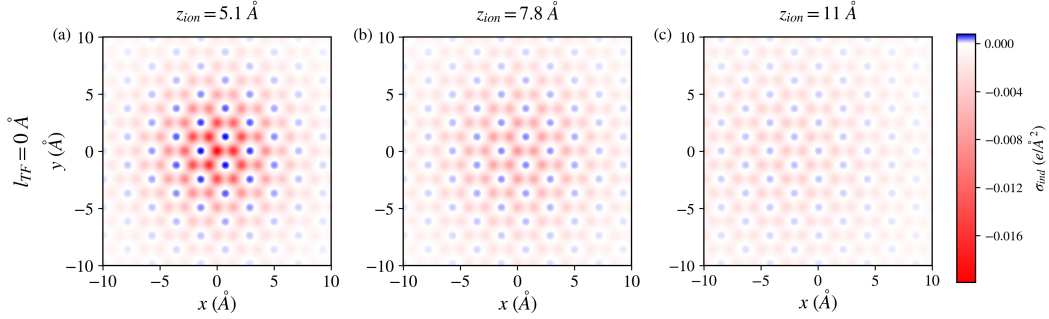
FIG. 2. Surface charge density $\sigma_{ind}(x, y)$ (see Eq. 10) induced in the graphite electrode, described as a perfect metal ($l_{TF} = 0$ Å), by an ion located at $(x, y) = (0, 0)$ and a distance from the first atomic plane of the electrode $z_{ion} = 5.1, 7.8$ and 11 Å for panels (a), (b) and (c), respectively. The colormap is common for the 3 panels. The slightly positively charged regions (blue) correspond to atoms in the second atomic plane of the electrode.

picture, which will be discussed in more detail below, the lateral decay of the charge is slower as l_{TF} increases, resulting in a more homogeneous charge distribution. This is also in line with the increase with l_{TF} of the correlation length observed in the surface charge induced in a capacitor consisting in an aqueous NaCl solution between graphite electrodes [64]. Such charge correlations within the electrode can be understood as resulting from the energetic cost of localizing the charge on each atom, evident in the second term in the r.h.s. Eq. 9, which entails an energy penalty $\propto l_{TF}^2 \sum_i q_i^2$ in Eq. 7. This penalization of large local charges also results in the absence of positively charged regions in panels 3b and 3c, which originated in the second plane due to the high local charge in the first plane for $l_{TF} = 0$.

B. Quantitative analysis with radial distribution of the induced charge

1. Effect of periodic boundary conditions

For the quantitative comparison of the results from atomistic calculations with analytical predictions, it is important to acknowledge the effect of periodic boundary conditions. This effect was already emphasized in Ref. [68] for gold electrodes with $l_{TF} = 0$, where it was taken into account by summing over periodic images their contribution in real space, Eq. 2. Since we don't know analytically the corresponding real-space expression for finite l_{TF}, in the present work we use instead the solution for the periodic case expressed as a sum over
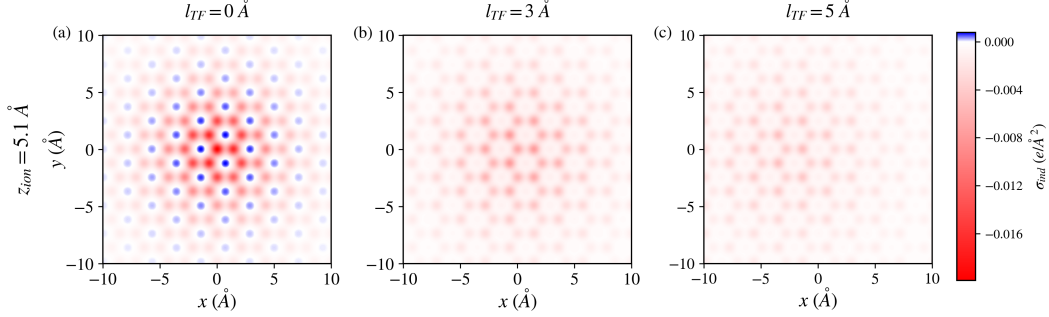
FIG. 3. Surface charge density $\sigma_{ind}(x, y)$ (see Eq. 10) induced in the graphite electrode by an ion located at $(x, y) = (0, 0)$ and a distance $z_{ion} = 5.1$ Å from the first atomic plane of the electrode, for Thomas-Fermi lengths $l_{TF} = 0, 3$ and 5 Å in panels (a), (b) and (c), respectively. The colormap is common for the 3 panels and the same as in Fig. 2.

modes, Eq. 4. We illustrate the effect of PBCs in the $l_{TF} = 0$ case, for which the periodic solution can be expressed as the $k_{TF} \to \infty$ limit of Eq. 4:

$$\sigma_{ind}^{l_{TF}=0}(x, y) = \frac{-q_{ion}}{L_x L_y} \sum_{m=0}^{\infty} \sum_{n=0}^{\infty} a_{m,n} e^{-k_{m,n}d} \cos(k_m x) \cos(k_n y) \tag{11}$$

with the same definition of the wavevectors k_m, k_n and $k_{m,n}$ and weights $a_{m,n}$. It is possible to show that in the limit $L_x, L_y \to \infty$, replacing the discrete sum by an integral and using polar coordinates, one recovers the solution for a single charge Eq. 2 with $r = \sqrt{x^2 + y^2}$.

The analytical predictions for both the single charge and periodic cases correspond to Eqs. 2 and 11 require the knowledge of the distance d of the ion from the interface. This is an important issue, discussed in more detailed below. Here we simply use $d = z_{ion}$, *i.e.* the distance of the ion from the first atomic plane of the electrode. As shown in Fig. 4 the radially averaged surface charge density $\sigma_{ind}(r)$ for $l_{TF} = 0$ and $z_{ion} = 5.1$ Å obtained from the atomistic description is well described (except for the oscillations due to the graphite lattice) by the analytical solution Eq. 11 for the periodic case over the whole r range. Expectedly, this is not the case for the single-charge result Eq. 4 which deviates from the numerical results at large distance. In the following, we therefore only consider the periodic solution Eq. 4 (and Eq. 11 for $l_{TF} = 0$).
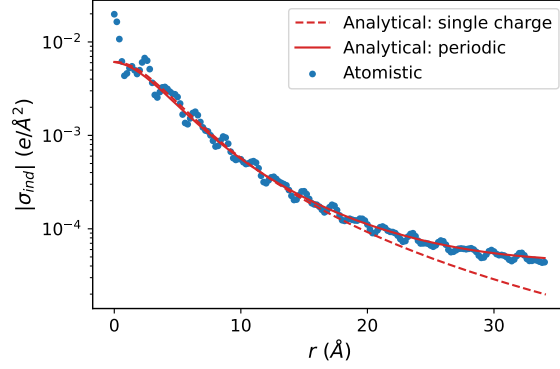
12

FIG. 4. Radially averaged surface charge density $\sigma_{ind}(r)$ (see Eq. 5) induced in the graphite electrode, described as a perfect metal ($l_{TF} = 0$ Å), by an ion located at $(x, y) = (0, 0)$ and a distance from the first atomic plane of the electrode $z_{ion} = 5.1$ Å. The results obtained within the atomistic description (symbols) are compared with the analytical prediction for a single charge (Eq. 2, dashed line) and that taking into account the periodic boundary conditions via Eq. 4 (solid line).

2. Effect of ion-surface distance for a perfect metal

As evident from Eq. 2, the induced charge distribution is expected to depend on the distance of the ion from the interface. Fig. 5 reports the atomistic prediction for $\sigma_{ind}(r)$ for $l_{TF} = 0$ and various positions z_{ion} of the ion, as well as the corresponding radial integrals $Q_{ind}(r)$ (see Eq. 6) in panels (a) and (b), respectively. In both panels, we also indicate the analytical predictions Eq. 2 using $d = z_{ion}$ as the distance from the interface. As already reported for a gold electrode in Ref. [68], Eq. 2 expectedly fails to capture the oscillations of $\sigma_{ind}(r)$, which are due to the atomic structure of the electrode (this point will be further examined in Section III C). These oscillations are averaged out in the radial integral, which is very well described by the analytical prediction from continuum electrostatics. We note that the charge does not integrate to $-q_{ion}$ because the radial integral doesn't include the corners of the simulation box. As can be easily checked using Eqs. 16 and 17 below, the total charge integrated over the whole surface is $\tilde{\sigma}_{ind}(k_m = 0, k_n = 0) \times L_x L_y = -q_{ion}$, as expected. Increasing the distance of ion from the surface decreases the local charge below the ion ($r = 0$) and increases the lateral extent of the charge distribution (with characteristic length d in the non-periodic case).
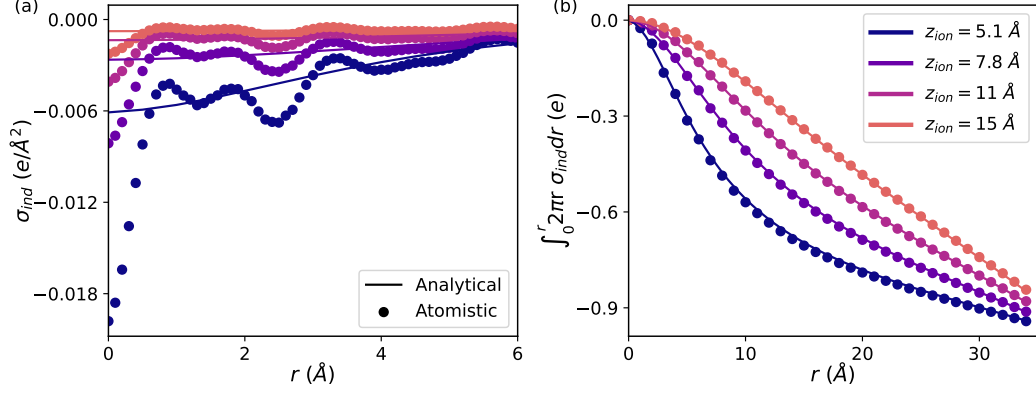
13

FIG. 5. (a) Radially averaged surface charge density $\sigma_{ind}(r)$ (see Eq. 5) induced in the graphite electrode, described as a perfect metal ($l_{TF} = 0$ Å), by an ion located at $(x, y) = (0, 0)$ and a distance from the first atomic plane of the electrode $z_{ion} = 5.1, 7.8, 11$ and 15 Å indicated by the colors in panel (b). The results obtained within the atomistic description (symbols) are compared with the analytical prediction taking into account the periodic boundary conditions via Eq. 4 (solid lines). (b) Running integral of the charge densities shown in the previous panel (see Eq. 6).

3. Effect of the Thomas-Fermi screening length

We now turn to the effect, which was not considered previously, of the Thomas-Fermi screening length on $\sigma_{ind}(r)$. Fig. 6 reports the atomistic prediction for $z_{ion} = 5.1$ Å and three values of l_{TF} (0, 3 and 5 Å), as well as the corresponding radial integrals $Q_{ind}(r)$ (see Eq. 6), in panels (a) and (b), respectively. Qualitatively, comparison with Fig. 5 suggests that the effect of increasing l_{TF} is similar to that of increasing the distance d from the ion, with a decrease of the local charge below the ion ($r = 0$) and an increase of the lateral extent of the charge distribution.

For a quantitative analysis, both panels in Fig. 6 also report the results from the continuum prediction, namely for finite l_{TF} the radial average Eq. 5 of Eq. 4 and the corresponding running integral Eq. 6. As in the $l_{TF} = 0$ case, the continuum prediction fails to account for the oscillations due to the atomic lattice. In addition, the predictions using $d = z_{ion}$ as the distance from the interface, which quantitatively agrees with the atomistic result for $l_{TF} = 0$, underestimates the magnitude of the local charge close to the ion and overestimates the extent of the lateral distribution.

Scalfi *et al.* showed in Ref. [62] that in order to quantitatively describe the capacitance per
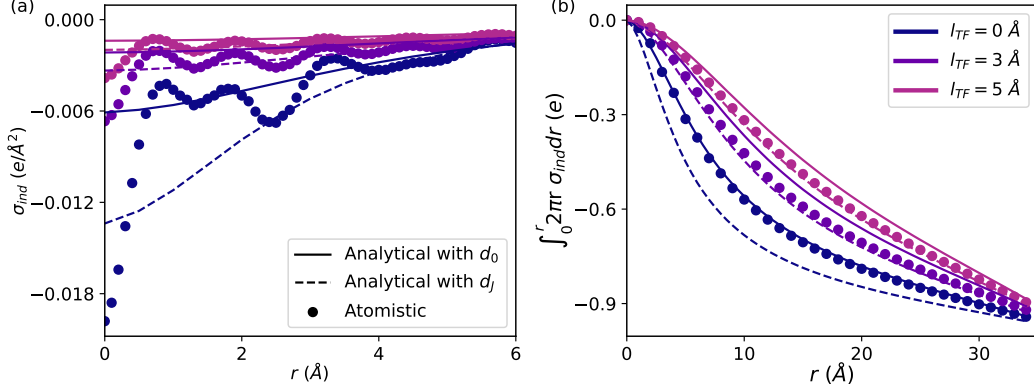
FIG. 6. (a) Radially averaged surface charge density $\sigma_{ind}(r)$ (see Eq. 5) induced in the graphite electrode by an ion located at $(x, y) = (0, 0)$ and a distance $z_{ion} = 5.1$ Å from the first atomic plane of the electrode, for Thomas-Fermi lengths $l_{TF} = 0, 3$ and 5 Å indicated by the colors in panel (b). The results obtained within the atomistic description (MD, symbols) are compared with the analytical prediction taking into account the periodic boundary conditions via Eq. 4, considering the position of the interface to be located at the first atomic plane (solid lines) or at the Jellium edge (dashed lines), see Eq. 12 and panel 1d. (b) Running integral of the charge densities shown in the previous panel (see Eq. 6).

unit area of empty capacitors by ϵ_0/L_{vac}, with L_{vac} the width of the vacuum slab between the electrodes, for finite l_{TF} one must consider that the interface between the metal and vacuum (the so-called "Jellium edge") is located away from the first atomic plane of the electrode, at a distance $z_J = a/2$, with a the interplane distance within the electrode (see Fig. 1d). One can therefore distinguish two predictions corresponding to the same model with two definitions of the position of the interface, $z_{int}^0 = 0$ and $z_{int}^J = z_J$ corresponding to the first atomic plane and to the Jellium edge, respectively, leading to different definitions of the ion-surface distance:

$$\begin{cases} d_0 = z_{ion} - z_{int}^0 = z_{ion} \\ d_J = z_{ion} - z_{int}^J = z_{ion} - a/2 \end{cases} \qquad (12)$$

Both panels of Fig. 6 include the analytical predictions using Eq. 4 with d_0 and d_J as solid and dashed lines, respectively. The definition d_J provides a better agreement with the numerical results, in particular for the radial integral in panel 6b, when the Thomas-Fermi length is comparable to or larger than the distances between atoms (d_{CC} within planes and

15

a between planes), while d_0 is more accurate for $l_{TF} = 0$ (d_J overestimates the local charge and underestimates the lateral extent in that case). The definition of the interface position will be further discussed in Section III C 3.

C. Quantitative analysis in reciprocal space

1. Definition of a characteristic decay length

For a single charge, $\sigma_{ind}(r)$ decays to 0 sufficiently fast that a characteristic length for the lateral decay of the induced charge can be defined *e.g.* as:

$$\xi = \frac{\int_0^\infty r \, \sigma_{ind}(r) 2\pi r \, \mathrm{d}r}{\int_0^\infty \sigma_{ind}(r) 2\pi r \, \mathrm{d}r} \tag{13}$$

which simplifies using Eq. 2 to $\xi = d$ in the perfect metal case $l_{TF} = 0$. However, such a definition cannot be used for periodic systems, where the reciprocal space provides a more convenient way to express and analyze the data, as evident from the expression of the induced charge Eq. 4 as a sum over modes. In fact, Eq. 11 for $l_{TF} = 0$ can also be rewritten as a sum over periodic images of the contributions of the form Eq. 2 (this is how the periodic solution was computed numerically in Ref [68]). The presence of the exponential term $e^{-k_{m,n}d}$ results, in the limit $L_x, L_y \to \infty$ where the discrete sum can be replaced by an integral, in Eq. 2 for a single charge, because $d/(r^2 + d^2)^{3/2}$ is the inverse Hankel transform of e^{-kd}. The characteristic decay length can therefore also be defined from the behaviour in reciprocal space.

More precisely, and in line with the analysis of Vorotyntsev and Kornyshev [6] from the behaviour at large r, for finite l_{TF} we consider the corresponding $k \to 0$ behaviour of the induced surface charge density. Starting from Eq. 4, and assuming $k \ll \epsilon_1 k_{TF}/\epsilon_2$ (and $k \ll k_{TF}$, which is implied by the previous relation in the general case where $\epsilon_2 \geq \epsilon_1$) we approximate the prefactor of each mode as:

$$\sigma_{ind}(x, y) \approx \frac{-q_{ion}}{L_x L_y} \sum_{m=0}^\infty \sum_{n=0}^\infty a_{m,n} e^{-k_{m,n}d} \left(1 - \frac{\epsilon_1 k_{m,n}}{\epsilon_2 k_{TF}} \right) \cos(k_m x) \cos(k_n y)$$

$$\approx \frac{-q_{ion}}{L_x L_y} \sum_{m=0}^\infty \sum_{n=0}^\infty a_{m,n} e^{-k_{m,n}d_{eff}} \cos(k_m x) \cos(k_n y) \tag{14}$$

with an effective distance

$$d_{eff} = d + \frac{\epsilon_1 l_{TF}}{\epsilon_2} , \tag{15}$$

16

which in the present case where $\epsilon_1 = \epsilon_2$ simplifies to $d_{eff} = d + l_{TF}$. In the limit $L_x, L_y \to \infty$, this leads to approximating the exact solution for a single charge and finite l_{TF} by the solution for $l_{TF} = 0$, Eq. 2, with an effective distance d_{eff}. This approximation, which is expected to be more accurate at large than short distance r, is consistent with the qualitative observations of Section III B 3.

In order to examine the charge density in reciprocal space, we consider the Fourier coefficients:

$$\tilde{\sigma}_{ind}(k_m, k_n) = \frac{1}{L_x L_y} \int_0^{L_x} \int_0^{L_y} \sigma_{ind}(x, y) e^{i(k_m x + k_n y)} \, \mathrm{d}x \mathrm{d}y \tag{16}$$

where the wavevectors are the ones compatible with the periodicity of the system, defined below Eq. 4. In the continuum picture, the latter equation yields

$$\tilde{\sigma}_{ind}(k_m, k_n) = -\frac{q_{ion}}{L_x L_y} \frac{\epsilon_2 k_{TF}^2 e^{-k_{m,n} d}}{\sqrt{k_{m,n}^2 + k_{TF}^2} (\epsilon_1 k_{m,n} + \epsilon_2 \sqrt{k_{m,n}^2 + k_{TF}^2})} \tag{17}$$

which reduces to

$$\tilde{\sigma}_{ind}^{l_{TF}=0}(k_m, k_n) = -\frac{q_{ion}}{L_x L_y} e^{-k_{m,n} d} \tag{18}$$

for $l_{TF} = 0$. In the $k \to 0$ limit, Eq. 17 can be approximated by

$$\tilde{\sigma}_{ind}^{l_{TF}}(k_m, k_n) \approx -\frac{q_{ion}}{L_x L_y} e^{-k_{m,n} d_{eff}} \,, \tag{19}$$

with d_{eff} given by Eq. 15. For the atomistic results, the Fourier components can be computed numerically via 2D Fast Fourier Transform (FFT). In the continuum picture the induced charge is real and even with respect to both x and y, so that the Fourier coefficients are real and even with respect to k_m and k_n. In the atomistic case, the structure of the graphite lattice (see inset in panel 7b) results in both an even real part and an odd imaginary part. In the following, in order to compare the two levels of description we only report the real part, and further limit the range of wavevectors to $k_{m,n} \geq 0$.

2. 2D charge density in reciprocal space: perfect metal

Fig. 7 shows the real part of the Fourier coefficients for $z_{ion} = 5.1$ Å and $l_{TF} = 0$ Å, for $k_n = 0$ and $k_m = 0$ in panels 7a and 7b, respectively. In each panel, the wavevector is rescaled by $2\pi/b$, with b the relevant dimension of the unit cell of the graphite lattice, shown as dashed lines in the inset of panel 7b. In both directions, one observes three features:
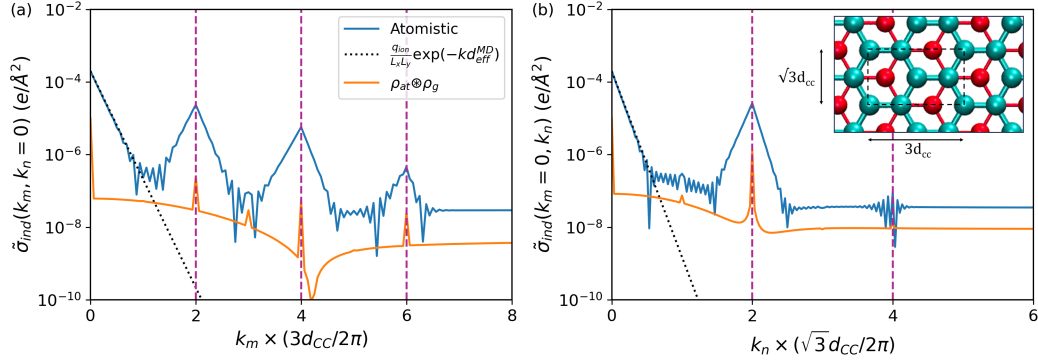
FIG. 7. Real part of the Fourier coefficients of the two-dimensional induced charge density, defined in Eq. 16, for $z_{ion} = 5.1$ Å and $l_{TF} = 0$ Å. Panel (a) corresponds to $\tilde{\sigma}_{ind}(k_m, k_n = 0)$, while panel (b) corresponds to $\tilde{\sigma}_{ind}(k_m = 0, k_n)$. In each panel, the wavevector is rescaled by $2\pi/b$, with b the relevant dimension of the unit cell of the graphite lattice. The latter is shown as dashed lines in the inset of panel (b), where cyan and red atoms correspond to the first and second atomic planes, respectively (half of the atoms in the second plane are hidden below atoms in the first plane). In both panels, the results from the atomistic description (blue solid line) are compared with the continuum prediction Eq. 18 with d fitted in the $k \to 0$ region to extract an effective distance d_{eff} (dotted lines). We also show (orange line) the Fourier coefficients of the convolution of the atomic number density ρ_{at} with the Gaussian charge density ρ_g for each atom (see text). The vertical dashed lines indicate even values of the abscissa.

(1) peaks at even multiples of $2\pi/b$, where $b = 3d_{CC}$ and $\sqrt{3}d_{CC}$ in the x and y directions, respectively; (2) wings decaying exponentially around each peak, appearing as straight lines on the semi-log plot (dotted lines in Fig. 7); (3) a baseline between the peaks.

The peaks reflect the discrete lattice structure, while the baseline is due to the Gaussian distribution of the charge around each atom. This can be confirmed by considering the density obtained by considering the atomic density ρ_{at} convoluted by the same Gaussian distribution ρ_g, i.e setting $q_i = 1$ for all atoms in Eq. 10. We estimate ρ_{at} numerically by summing over atoms in the first two planes (since two planes are needed to include the full graphite unit cell); to facilitate comparison with the charge distribution in the figure, we divide the result by the number of atoms in the two planes (since for $k = 0$ we expect $q_{ion}/L_x L_y$ for the charge density and $N_{at}/L_x L_y$ for the number density). Some (x_i, y_i) coordinates correspond to atoms in both atomic planes of the graphite unit cell (see the

18

inset in panel 7b). The Fourier coefficients of the convolution $\rho_{at} \circledast \rho_g$, shown as orange solid line in Fig. 7, reproduce the location of the peaks and the baseline. The magnitude of the peaks differs however from that of $\tilde{\sigma}_{ind}$ because the charge distribution is not identical to the atomic distribution.

Finally, in the $k \to 0$ limit the Fourier coefficients decay exponentially, consistently with Eq. 18, or more generally with Eq. 14. The slopes of the decay in the x and y directions result in the same effective decay lengths $d_{eff} = 4.8 \pm 0.1$ Å. This value is consistent with the distance $d_0 = 5.1$ Å for this case, even though slightly smaller. Possible deviations could be due to the breakdown of the continuum approximation for this relatively short distance compared to the molecular features of graphite (d_{CC} and corresponding unit cell parameters in the plane, a between planes), or to the Gaussian charge distribution on electrode atoms, as already noted for the effective distance necessary between electrodes to reproduce the capacitance of empty capacitors [60, 62].

3. Effect of the Thomas-Fermi screening length

We now turn to the case of a finite Thomas-Fermi screening length. Fig. 8a shows the Fourier coefficients for $z_{ion} = 7.8$ Å and $l_{TF} = 5$ Å, for $k_n = 0$. The results display the same features as in the $l_{TF} = 0$ case. The peaks and baseline are again consistent with the convolution of the atomic density with the Gaussian distribution assigned to each atom. The decay for small k is well described by an exponential, even though this behaviour is expected to be only approximate for finite l_{TF} (see Eq. 19) because it assumes $k \ll \epsilon_1 k_{TF}/\epsilon_2 = k_{TF}$ in the present case. The corresponding effective decay length, obtained by fitting the data by Eq. 19 for $k \to 0$, is $d_{eff}^{MD} = 12.3 \pm 0.2$ Å. Since the results of Section III B 3 suggest that the relevant ion-surface distance is that from the Jellium edge, we should compare this value with the prediction of Eq. 15 using $d = d_J$, which yields in that case $d_{eff} = 11.1$ Å. Even though the agreement is not perfect, this confirms the relevance of the continuum picture to describe the behaviour for small wavevectors, *i.e.* large distances.

This can be further illustrated in real space with the radial distribution $\sigma_{ind}(r)$. In Fig. 8b, the results from the atomistic description are compared with the continuum predictions using the exact 2D density Eq. 4, as well as the small k approximation Eqs. 14-15, using $d_{eff} = d_J + l_{TF}$ and from the fit in panel (a) of the atomistic results. As already discussed
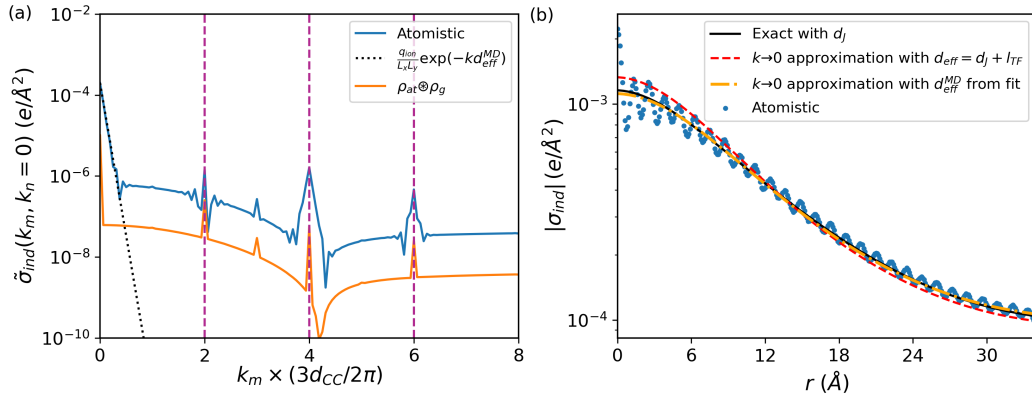
FIG. 8. (a) Real part fo the Fourier coefficients of the two-dimensional induced charge density, defined in Eq. 16, for $z_{ion} = 7.8$ Å, $l_{TF} = 5$ Å and $k_n = 0$. As in panel 7a, the wavector is rescaled by $2\pi/b$, with b the relevant dimension of the unit cell of the graphite lattice. The results from the atomistic description (blue solid line) are compared with the continuum approximation Eq. 19 with d fitted in the $k \to 0$ region to extract an effective distance d_{eff}^{MD} (dotted lines). We also show (orange line) the Fourier coefficients of the convolution of the atomic number density ρ_{at} with the Gaussian charge density ρ_g for each atom (see text). The vertical dashed lines indicate even values of the abscissa. (b) Radial distribution of the induced charged density $\sigma_{ind}(r)$ (see Eq. 5) for the same system. Results from the atomistic description (symbols) are compared with the continuum predictions using the exact 2D density Eq. 4 (black solid line), or the small k approximation Eqs. 14-15, using $d_{eff} = d_J + l_{TF}$ (red dashed line) or from the fit in panel (a) of the atomistic results (orange dashed-dotted line).

in Section III B 3, the full solution with $d = d_J$ provides an excellent agreement with the atomistic results, except for the oscillations arising from the lattice structure. Note that compared *e.g.* with Fig. 6a, the r range is significantly extended and the semi-logarithmic representation highlights the accuracy of the continuum prediction for large distances. The small $k \to 0$ approximation with $d_{eff} = d_J + l_{TF}$ is also in relatively good agreement with the atomistic results, even though it overestimates the charge at short distance and underestimates it at large distance. Surprizingly, the small $k \to 0$ approximation with d_{eff}^{MD} fitted from the Fourier coefficients at small k is in almost quantitative agreement with the exact result over the whole r range and not only for large distances corresponding to small wavevectors.

20

These observations support the idea that the finite l_{TF} case can be well approximated by the solution for a perfect metal, using an effective distance (in particular in Eq. 2 for a single charge) that depends on l_{TF}, reasonably described by Eq. 15. In order to further test this approximation for d_{eff}, we report it in Fig. 9a as a function of the ion position z_{ion} for l_{TF} between 0 and 5 Å. The lines indicate fits of the form $d_{eff} = z_{ion} - z_{int}^{eff} + l_{TF}$, which provide in each case an effective position of the interface consistent with the linear scaling with both z_{ion} and l_{TF}.
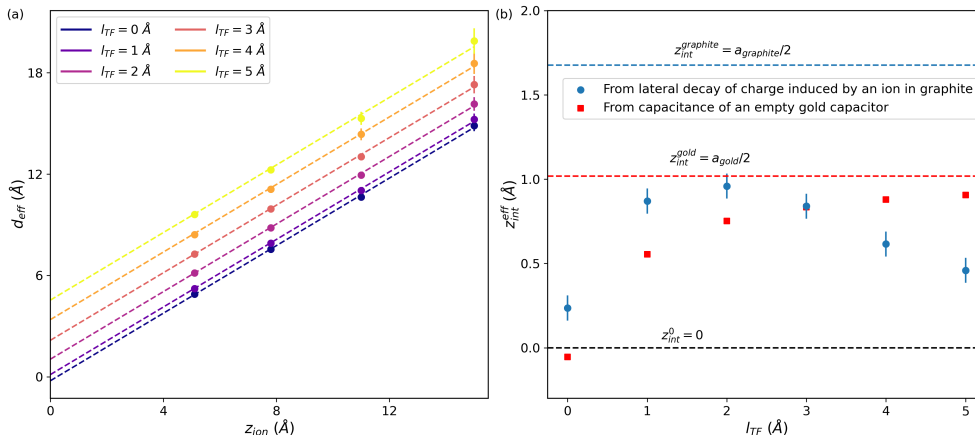

FIG. 9. (a) Effective decay length d_{eff}^{MD} obtained by fitting the $k \to 0$ behaviour of the Fourier coefficients of the induced charge density (see Figs. 7 and 8), as a function of the position of the ion z_{ion}, for l_{TF} ranging from 0 to 5 Å. The numerical results (symbols) are fitted to $d_{eff} = z_{ion} - z_{int}^{eff} + l_{TF}$ (dashed lines). (b) Effective position of the interface resulting from the fits of panel (a), as a function of the Thomas-Fermi screening length l_{TF} as symbols in panel (blue circles). Also shown in panel (b) is the same quantity deduced from the effective screening length introduced in Ref. [62] to account for the capacitance of empty capacitors with gold electrodes (red squares). The position of the Jellium edge is indicated as dashed horizontal lines for both graphite and gold electrodes.

This quantity is then shown in Fig. 9b as a function of l_{TF}. Consistently with the above results, z_{int}^{eff} is found to be between z_{int}^0 and $z_{int}^J = a/2$, with a value close to z_{int}^0 for $l_{TF} = 0$. In Ref. [62] introducing the Thomas-Fermi model in constant-potential simulations, Scalfi *et al.* considered the capacitance of empty gold capacitors with varying l_{TF}. They analyzed the results in terms of an equivalent circuit model consisting of capacitors in series, with capacitances per unit area ϵ_0/L_{vac} for the vacuum slab and ϵ_0/l_{eff} for each electrode, where

the width L_{vac} was taken as the distance between the two Jellium edges. The resulting effective screening length was found to coincide with l_{TF} for large screening lengths, but to deviate when the latter become comparable to the atomic distances within the electrode. In Fig. 9b, we also report the same results of Ref. [62] by adopting a different perspective, namely assuming that the capacitance inside the metal can be estimated using l_{TF} and that the capacitance of the whole system provides instead an effective vacuum slab width, which we translate in terms of the position of the interface. While the results are not identical with those obtained in the present work from the lateral decay of the charge induced by an ion, they share some similar features, such as being within half of the interplane distance from the first atomic plane, with a value close to z_{int}^0 for $l_{TF} = 0$.

The insertion of alkaline cations in narrow carbon and graphite nanotubes was investigated by Goduljan et $al.$ using DFT [76]. Even though it is not possible to define an effective image plane in this geometry, so that the authors "refrained from comparing [their] calculations with the results of a Thomas-Fermi model [12], which suffers from the same problem", they observed that the "image charge" resides on the atoms of the wall and extends toward the ion, with more delocalization in the case of gold compared to carbon, leading to a better screening of the electrostatic potential, as predicted by Rochester et $al.$ [12] and as expected for a better conductor. We reiterate that the definition of z_{int}^{eff} in the present work is based on an approximation only valid for $k \rightarrow 0$. In addition, it has been suggested in Ref. [60] that the effective distance between electrodes necessary to describe the capacitance might also be related to other parameters such as the width of the Gaussian charge distributions around each atom, which was shown to play an important role on the interfacial properties [43, 53, 67]. Nevertheless, this comparison for different systems and different definitions of the location of the interface lead to overall consistent conclusions.

IV. CONCLUSION

We have studied the charge induced in a Thomas-Fermi metal by an ion in vacuum, using an atomistic description employed in constant-potential molecular dynamics simulations, and compared the results with the (semi-)analytical predictions obtained from continuum electrostatics. Following a previous study for a gold electrode described as a perfect metal (with a Thomas-Fermi screening length $l_{TF} = 0$), with an ion in vacuum and in water, we

considered the effect of screening inside the metal by restricting ourselves to the case of an ion in vacuum near a graphite electrode, varying l_{TF} and the position of the ion with respect to the surface. Our analysis of the induced charge included not only 2D density maps and their radial averages, but also their Fourier coefficients in order to extract the long-range behaviour under the periodic boundary conditions inherent to molecular simulations. The comparison with the continuum picture also included new analytical results taking these periodic boundary conditions into account.

Overall, the continuum predictions capture most of the features observed with the atomistic description (except the oscillations due to the discrete atomic sites of the graphite lattice, as expected), provided that the distance of the ion from the surface and the Thomas-Fermi length are larger than the inter-atomic distances within the electrode. The analysis of the Fourier coefficients for small wavevectors shows that, at large distance, the finite l_{TF} case can be well approximated by the solution for a perfect metal, using an effective distance, reasonably described by the sum of the distance between the ion and the Jellium edge (which corresponds to the electrode/vacuum interface) and the Thomas-Fermi screening length. Surprisingly, we find that this approximation is in fact rather accurate even at intermediate and short distances. The linear relation between the effective distance and both the ion position and the screening length can also be translated in terms of an effective position of the interface, which depends on l_{TF}, is within half of the interplane distance from the first atomic plane of the electrode, and is broadly consistent with another definition from the capacitance of empty capacitors.

These conclusions support in particular an early analytical prediction by Vorotyntsev and Kornyshev for a single charge (nonperiodic case) located at the interface between a Thomas-Fermi metal and a polarizable medium. We are currently exploring the effect of the interplay between screening within the metal and by a polar solvent on the charge induced by an ion, using molecular simulations. Further studies could also include the interplay with screening by ions in an electrolyte, in order to provide simple analytical approximations in that case, which is the most relevant for practical applications of electrode/electrolyte interfaces, including the effect of voltage (which cannot be applied in the case of a single electrode). Finally, a comparative study of related approaches to describe electronic effects in classical molecular simulations (*e.g.* tuning the Thomas-Fermi screening length [62, 64], or Gaussian width [53, 67] in constant-potential simulations, or constant-electrochemical potential [43]

simulations) would be useful for the community investigating electrochemical interfaces from this point of view, and to make more explicit connections with that approaching them using *ab initio* simulations.

ACKNOWLEDGEMENTS

APPENDIX

As indicated in Section II, the ionic positions z_{ion} considered in the present work were chosen based on the equilibrium density profile of Na^+ at the interface between graphite and a 1 M NaCl aqueous solution using the same model. The corresponding simulations were performed with the force field described in the main text and the SPC/E water model [77], with the system illustrated in Fig. 10a. It contains 2 graphite electrodes (with $l_{TF} = 0$), each consisting of 1440 atoms in 3 planes, maintained at the same potential (*i.e.* a voltage $\Delta\psi = 0$ V), as well as 2160 water molecules and 39 ion pairs. The box dimensions are $L_x = 34.10$ Å, $L_y = 36.91$ Å and $L_z = 211.67$ Å, and periodic boundary conditions are applied only in the x and y directions. Newton's equations of motion are integrated using a time step of 1 fs. The system is first equilibrated during 0.5 ns in the NPT ensemble at a pressure of 1 atm by applying a corresponding force on the electrodes (pistons) and a temperature $T = 298$ K by applying a Nosé-Hoover chain thermostat with a time constant of 1 ps. The distance between the first atomic plane of the electrodes is then fixed (to 56.268 Å) for subsequent runs in the NVT ensemble. After 0.5 ns of equilibration, a production run of

24

8 ns is performed, sampling the configurations every 1 ps to compute the equilibrium density profiles of water oxygen and hydrogen atoms (see Fig. 10b) and sodium and chloride ions (see Fig. 10c). The vertical dashed lines in panel Fig. 10c indicate the selected positions for the present study of an ion in vacuum.
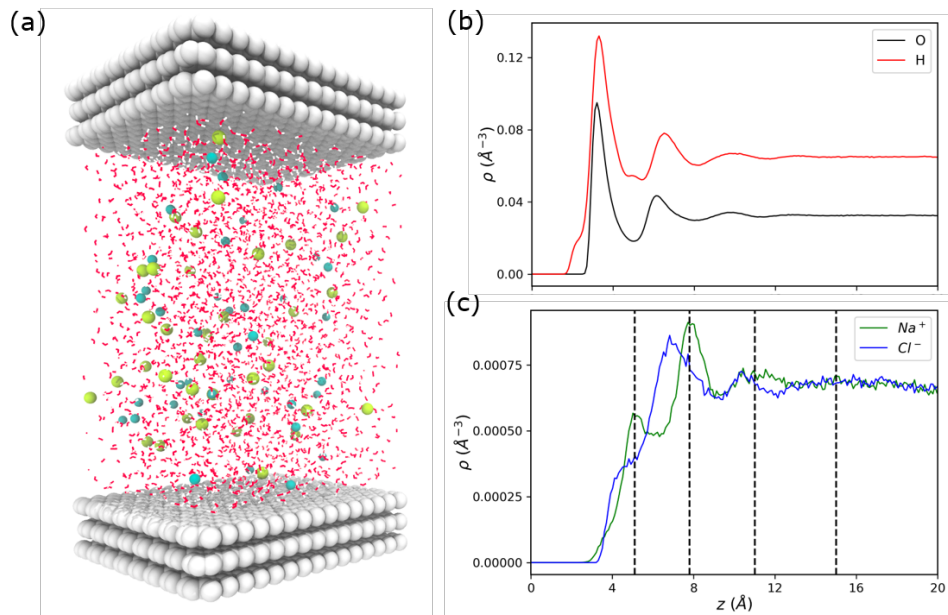

FIG. 10. (a) Simulated system for a 1 M NaCl aqueous solution between graphite electrodes. Equilibrium density profiles for water and ions are shown in panels (b) and (c), respectively. The vertical dashed lines in panel (c) indicate the selected positions for the present study of an ion in vacuum.

[1] L.H. Thomas. The calculation of atomic fields. *Proc. Cambridge Phil. Roy. Soc.*, 23:542–548, 1927.

[2] E. Fermi. Un metodo statistico per la determinazione di alcune proprietà dell'atomo. *Rend. Accad. Naz. Lincei*, 6:602–607, 1927.

[3] Neil W Ashcroft and N David Mermin. *Solid state physics*. Holt, Rinehart and Winston, New York, NY, 1976.

[4] A. A. Kornyshev, A. I. Rubinshtein, and M. A. Vorotyntsev. Image potential near a dielectric–plasma-like medium interface. *physica status solidi (b)*, 84(1):125–132, 1977.

[5] A. A. Kornyshev and M. A. Vorotyntsev. Analytic expression for the potential energy of atest charge bounded by solid state plasma. *J. Phys. C: Solid State Phys.*, 11:L691–L694, 1978.

[6] M. A. Vorotyntsev and A. A. Kornyshev. Electrostatic interaction on a metal-insulator interface. *Soviet Journal of Experimental and Theoretical Physics*, 51:509, March 1980.

[7] A. A. Kornyshev, W. Schmickler, and M. A. Vorotyntsev. Nonlocal electrostatic approach to the problem of a double layer at a metal-electrolyte interface. *Phys. Rev. B*, 25:5244–5256, 1982.

[8] P G Dzhavakhidze, A A Kornyshev, and L I Krishtalik. Activation energy of electrode reactions: the non-local effects. *J. Electroanal. Chem.*, 228:329–346, 1987.

[9] D. K. Phelps, A. A. Kornyshev, and M. J. Weaver. Nonlocal Electrostatic Effects on Electron-Transfer Activation Energies: Some Consequences for and Comparisons with Electrochemical and Homogeneous-Phase Kinetics. *J. Phys. Chem.*, 94:1454–1463, 1990.

[10] N. B. Luque and W. Schmickler. The electric double layer on graphite. *Electrochim. Acta*, 71:82–85, 2012.

[11] A. A. Kornyshev, N. B. Luque, and W. Schmickler. Differential capacitance of ionic liquid interface with graphite: the story of two double layers. *J. Solid State Electrochem.*, 18:1345–1349, 2014.

[12] C. C. Rochester, A. A. Lee, G. Pruessner, and A. A. Kornyshev. Interionic interactions in conducting nanoconfinement. *ChemPhysChem*, 14:4121–4125, 2013.

[13] J. Comtet, A. Niguès, V. Kaiser, B. Coasne, L. Bocquet, and A. Siria. Nanoscale capillary freezing of ionic liquids confined between metallic interfaces and the role of electronic screening.

Nat. Mater., 16:634–639, 2017.

[14] V. Kaiser, J. Comtet, A. Niguès, A. Siria, B. Coasne, and L. Bocquet. Electrostatic interactions between ions near thomas–fermi substrates and the surface energy of ionic crystals at imperfect metals. *Faraday Discuss.*, 199:129–158, 2017.

[15] N. D. Lang and W. Kohn. Theory of metal surfaces: Induced surface charge and image potential. *Phys. Rev. B*, 7:3541–3550, Apr 1973.

[16] Wolfgang Schmickler and Douglas Henderson. The interphase between jellium and a hard sphere electrolyte. A model for the electric double layer. *The Journal of Chemical Physics*, 80(7):3381–3386, April 1984. Publisher: American Institute of Physics.

[17] N. V. Smith, C. T. Chen, and M. Weinert. Distance of the image plane from metal surfaces. *Phys. Rev. B*, 40:7565–7573, Oct 1989.

[18] J Jung, J E Alvarellos, E Chacón, and P García-González. Self-consistent density functional calculation of the image potential at a metal surface. 19(26):266008, jun 2007.

[19] E. K. Yu, D. A. Stewart, and S. Tiwari. Ab initio study of polarizability and induced charge densities in multilayer graphene films. *Phys. Rev. B*, 77:195406, May 2008.

[20] Sandeep Tyagi, Axel Arnold, and Christian Holm. ICMMM2D: An accurate method to include planar dielectric interfaces via image charge summation. *J. Chem. Phys.*, 127(15):154723, October 2007.

[21] Sandeep Tyagi, Axel Arnold, and Christian Holm. Electrostatic layer correction with image charges: A linear scaling method to treat slab 2D+h systems with dielectric interfaces. *J. Chem. Phys.*, 129(20):204102, November 2008. Publisher: American Institute of Physics.

[22] A. Arnold, K. Breitsprecher, F. Fahrenberger, S. Kesselheim, O. Lenz, and C. Holm. Efficient algorithms for electrostatic interactions including dielectric contrasts. *Entropy*, 15:4569–4588, 2013.

[23] Matheus Girotto, Alexandre P. dos Santos, and Yan Levin. Simulations of ionic liquids confined by metal electrodes using periodic Green functions. *The Journal of Chemical Physics*, 147(7):074109, August 2017.

[24] Trung Dac Nguyen, Honghao Li, Debarshee Bagchi, Francisco J. Solis, and Monica Olvera de la Cruz. Incorporating surface polarization effects into large-scale coarse-grained Molecular Dynamics simulation. *Computer Physics Communications*, 241:80–91, August 2019.

[25] Ondrej Maxian, Raúl P. Peláez, Leslie Greengard, and Aleksandar Donev. A fast spectral method for electrostatics in doubly periodic slit channels. *The Journal of Chemical Physics*, 154(20):204107, May 2021. Publisher: American Institute of Physics.

[26] Jiaxing Yuan, Hanne S. Antila, and Erik Luijten. Particle–particle particle–mesh algorithm for electrolytes between charged dielectric interfaces. *The Journal of Chemical Physics*, 154(9):094115, March 2021. Publisher: American Institute of Physics.

[27] A. P. dos Santos, F. Jiménez-Ángeles, A. Ehlen, and M. Olvera de la Cruz. Modulation of ionic conduction using polarizable surfaces. *Physical Review Research*, 5(4):043174, November 2023. Publisher: American Physical Society.

[28] Sung Sakong and Axel Groß. The electric double layer at metal-water interfaces revisited based on a charge polarization scheme. *J. Chem. Phys.*, 149(8):084705, August 2018.

[29] Joshua D. Elliott, Alessandro Troisi, and Paola Carbone. A QM/MD Coupling Method to Model the Ion-Induced Polarization of Graphene. *Journal of Chemical Theory and Computation*, 16(8):5253–5263, August 2020. Publisher: American Chemical Society.

[30] Jia-Bo Le, Ao Chen, Lang Li, Jing-Fang Xiong, Jinggang Lan, Yun-Pei Liu, Marcella Iannuzzi, and Jun Cheng. Modeling Electrified Pt(111)-Had/Water Interfaces from Ab Initio Molecular Dynamics. *JACS Au*, 1(5):569–577, May 2021. Publisher: American Chemical Society.

[31] Sung Sakong, Jun Huang, Michael Eikerling, and Axel Groß. The structure of the electric double layer: Atomistic versus continuum approaches. *Current Opinion in Electrochemistry*, 33:100953, June 2022.

[32] Ken Takahashi, Hiroshi Nakano, and Hirofumi Sato. Accelerated constant-voltage quantum mechanical/molecular mechanical method for molecular systems at electrochemical interfaces. *The Journal of Chemical Physics*, 157(23):234107, December 2022. Publisher: American Institute of Physics.

[33] Ravishankar Sundararaman, Derek Vigil-Fowler, and Kathleen Schwarz. Improving the Accuracy of Atomistic Simulations of the Electrochemical Interface. *Chemical Reviews*, 122(12):10651–10674, June 2022. Publisher: American Chemical Society.

[34] Andrea Grisafi, Augustin Bussy, Mathieu Salanne, and Rodolphe Vuilleumier. Predicting the charge density response in metal electrodes. *Physical Review Materials*, 7(12):125403, December 2023. Publisher: American Physical Society.

[35] J. Ilja Siepmann and Michiel Sprik. Influence of surface topology and electrostatic potential on water/electrode systems. *The Journal of Chemical Physics*, 102(1):511–524, 01 1995.

[36] E. Spohr. Molecular simulation of the electrochemical double layer. *Electrochimica Acta*, 44(11):1697–1705, 1999.

[37] Alexei A. Kornyshev, Eckhard Spohr, and Michael A. Vorotyntsev. *Electrochemical Interfaces: At the Border Line*, pages 33–132. John Wiley & Sons, Ltd, 2007.

[38] Stewart K. Reed, Paul A. Madden, and Aristides Papadopoulos. Electrochemical charge transfer at a metallic electrode: A simulation study. *The Journal of Chemical Physics*, 128(12), 03 2008. 124701.

[39] M. V. Fedorov and A. A. Kornyshev. Ionic liquids at electrified interfaces. *Chem. Rev.*, 114:2978—3036, 2014.

[40] Nicolas Onofrio and Alejandro Strachan. Voltage equilibration for reactive atomistic simulations of electrochemical processes. *The Journal of Chemical Physics*, 143(5):054109, August 2015.

[41] Konrad Breitsprecher, Kai Szuttor, and Christian Holm. Electrode Models for Ionic Liquid-Based Capacitors. *J. Phys. Chem. C*, 119(39):22445–22451, October 2015.

[42] Tao Liang, Andrew C. Antony, Sneha A. Akhade, Michael J. Janik, and Susan B. Sinnott. Applied Potentials in Variable-Charge Reactive Force Fields for Electrochemical Systems. *J. Phys. Chem. A*, 122(2):631–638, January 2018.

[43] Hiroshi Nakano and Hirofumi Sato. A chemical potential equalization approach to constant potential polarizable electrodes for electrochemical-cell simulations. *The Journal of Chemical Physics*, 151(16):164123, October 2019.

[44] Ken Takahashi, Hiroshi Nakano, and Hirofumi Sato. Unified polarizable electrode models for open and closed circuits: Revisiting the effects of electrode polarization and different circuit conditions on electrode–electrolyte interfaces. *The Journal of Chemical Physics*, 157(1):014111, July 2022.

[45] Ranisha S. Sitlapersad, Anthony R. Thornton, and Wouter K. den Otter. A simple efficient algorithm for molecular simulations of constant potential electrodes. *The Journal of Chemical Physics*, 160(3):034107, January 2024.

[46] Laura Scalfi, Mathieu Salanne, and Benjamin Rotenberg. Molecular Simulation of Electrode-Solution Interfaces. *Annual Review of Physical Chemistry*, 72(1):189, April 2021.

[47] Guillaume Jeanmairet, Benjamin Rotenberg, and Mathieu Salanne. Microscopic Simulations of Electrochemical Double-Layer Capacitors. *Chemical Reviews*, 122(12):10860–10898, June 2022. Publisher: American Chemical Society.

[48] A. P. Willard, S. K. Reed, P. A. Madden, and D. Chandler. Water at an electrochemical interface - a simulation study. *Faraday Discuss.*, 141:423–441, 2009.

[49] D. T. Limmer, A. P. Willard, P. Madden, and D. Chandler. Hydration of metal surfaces can be dynamically heterogeneous and hydrophobic. *Proc. Natl. Acad. Sci. U.S.A.*, 110:4200–4205, 2013.

[50] A. P. Willard, D. T. Limmer, P. A. Madden, and D. Chandler. Characterizing heterogeneous dynamics at hydrated electrode surfaces. *J. Chem. Phys.*, 138:184702, 2013.

[51] E. Paek, A. J. Pak, and G. S. Hwang. On the influence of polarization effects in predicting the interfacial structure and capacitance of graphene-like electrodes in ionic liquids. *J. Chem. Phys.*, 142:024701, 2015.

[52] M. Buraschi, S. Sansotta, and D. Zahn. Polarization effects in dynamic interfaces of platinum electrodes and ionic liquid phases: A molecular dynamics study. *J. Phys. Chem. C*, 124:2002–2007, 2020.

[53] Alessandra Serva, Laura Scalfi, Benjamin Rotenberg, and Mathieu Salanne. Effect of the metallicity on the capacitance of gold–aqueous sodium chloride interfaces. *The Journal of Chemical Physics*, 155(4):044703, July 2021. Publisher: American Institute of Physics.

[54] Philip Loche, Laura Scalfi, Mustakim Ali Amu, Otto Schullian, Douwe J. Bonthuis, Benjamin Rotenberg, and Roland R. Netz. Effects of surface rigidity and metallicity on dielectric properties and ion interactions at aqueous hydrophobic interfaces. *The Journal of Chemical Physics*, 157(9):094707, September 2022. Publisher: American Institute of Physics.

[55] Samuel Ntim and Marialore Sulpizi. Role of image charges in ionic liquid confined between metallic interfaces. *Physical Chemistry Chemical Physics*, 22(19):10786–10791, May 2020. Publisher: The Royal Society of Chemistry.

[56] Samuel Ntim and Marialore Sulpizi. Molecular dynamics simulations of electrified interfaces including the metal polarisation. *Physical Chemistry Chemical Physics*, July 2023. Publisher: The Royal Society of Chemistry.

[57] Samuel Ntim and Marialore Sulpizi. Differential Capacitance of Ionic Liquid Confined between Metallic Interfaces. *The Journal of Physical Chemistry B*, February 2024. Publisher: American

Chemical Society.

[58] D. T. Limmer, C. Merlet, M. Salanne, D. Chandler, P. A. Madden, R. van Roij, and B. Rotenberg. Charge fluctuations in nanoscale capacitors. *Phys. Rev. Lett.*, 111:106102, 2013.

[59] Céline Merlet, David T. Limmer, Mathieu Salanne, René van Roij, Paul A. Madden, David Chandler, and Benjamin Rotenberg. The Electric Double Layer Has a Life of Its Own. *The Journal of Physical Chemistry C*, 118(32):18291–18298, August 2014.

[60] Laura Scalfi, David T. Limmer, Alessandro Coretti, Sara Bonella, Paul A. Madden, Mathieu Salanne, and Benjamin Rotenberg. Charge fluctuations from molecular simulations in the constant-potential ensemble. *Physical Chemistry Chemical Physics*, 22(19):10480–10489, May 2020.

[61] Giovanni Pireddu and Benjamin Rotenberg. Frequency-dependent impedance of nanocapacitors from electrode charge fluctuations as a probe of electrolyte dynamics. *Phys. Rev. Lett.*, 130:098001, Feb 2023.

[62] Laura Scalfi, Thomas Dufils, Kyle G. Reeves, Benjamin Rotenberg, and Mathieu Salanne. A semiclassical thomas–fermi model to tune the metallicity of electrodes in molecular simulations. *The Journal of Chemical Physics*, 153(17):174704, 2020.

[63] Alexander Schlaich, Dongliang Jin, Lyderic Bocquet, and Benoit Coasne. Electronic screening using a virtual Thomas–Fermi fluid for predicting wetting and phase transitions of ionic liquids at metal surfaces. *Nature Materials*, November 2021.

[64] Laura Scalfi and Benjamin Rotenberg. Microscopic origin of the effect of substrate metallicity on interfacial free energies. *Proceedings of the National Academy of Sciences*, 118(50):e2108769118, 2021.

[65] Yun Yu, Kaidi Zhang, Holden Parks, Mohammad Babar, Stephen Carr, Isaac M. Craig, Madeline Van Winkle, Artur Lyssenko, Takashi Taniguchi, Kenji Watanabe, Venkatasubramanian Viswanathan, and D. Kwabena Bediako. Tunable angle-dependent electrochemistry at twisted bilayer graphene with moiré flat bands. *Nature Chemistry*, 14(3):267–273, March 2022.

[66] Leonardo Coello Escalante and David T. Limmer. Microscopic origin of twist-dependent electron transfer rate in bilayer graphene, 2024.

[67] Kateryna Goloviznina, Johann Fleischhaker, Tobias Binninger, Benjamin Rotenberg, Heigo Ers, Vladislav Ivanistsev, Robert Meissner, Alessandra Serva, and Mathieu Salanne. Accounting for the quantum capacitance of graphite in constant potential molecular dynamics

simulations, 2024.

[68] Giovanni Pireddu, Laura Scalfi, and Benjamin Rotenberg. A molecular perspective on induced charges on a metallic surface. *The Journal of Chemical Physics*, 155(20):204705, 2021.

[69] J. D. Jackson. *Electrodynamics, Classical.* John Wiley & Sons, Ltd, 2003.

[70] S. K. Reed, O. J. Lanning, and P. A. Madden. Electrochemical Interface Between an Ionic Liquid and a Model Metallic Electrode. *J. Chem. Phys.*, 126:084704, 2007.

[71] Abel Marin-Laflèche, Matthieu Haefele, Laura Scalfi, Alessandro Coretti, Thomas Dufils, Guillaume Jeanmairet, Stewart K. Reed, Alessandra Serva, Roxanne Berthin, Camille Bacon, Sara Bonella, Benjamin Rotenberg, Paul A. Madden, and Mathieu Salanne. MetalWalls: A classical molecular dynamics software dedicated to the simulation of electrochemical systems. *Journal of Open Source Software*, 5(53):2373, September 2020.

[72] Alessandro Coretti, Camille Bacon, Roxanne Berthin, Alessandra Serva, Laura Scalfi, Iurii Chubak, Kateryna Goloviznina, Matthieu Haefele, Abel Marin-Laflèche, Benjamin Rotenberg, Sara Bonella, and Mathieu Salanne. MetalWalls: Simulating electrochemical interfaces between polarizable electrolytes and metallic electrodes. *The Journal of Chemical Physics*, 157(18):184801, November 2022. Publisher: American Institute of Physics.

[73] Ludwig J. V. Ahrens-Iwers, Mathijs Janssen, Shern R. Tee, and Robert H. Meißner. ELEC-TRODE: An electrochemistry package for atomistic simulations. *The Journal of Chemical Physics*, 157(8):084801, August 2022. Publisher: American Institute of Physics.

[74] Liem X. Dang. Mechanism and thermodynamics of ion selectivity in aqueous solutions of 18-crown-6 ether: A molecular dynamics study. *Journal of the American Chemical Society*, 117(26):6954–6960, 1995.

[75] T. Werder, J. H. Walther, R. L. Jaffe, T. Halicioglu, and P. Koumoutsakos. On the water-carbon interaction for use in molecular dynamics simulations of graphite and carbon nan-otubes. *The Journal of Physical Chemistry B*, 107(6):1345–1352, 2003.

[76] Aleksej Goduljan, Fernanda Juarez, Leila Mohammadzadeh, Paola Quaino, Elizabeth Santos, and Wolfgang Schmickler. Screening of ions in carbon and gold nanotubes — a theoretical study. *Electrochemistry Communications*, 45:48–51, 2014.

[77] H. J. C. Berendsen, J. R. Grigera, and T. P. Straatsma. The missing term in effective pair potentials. *Journal of Physical Chemistry*, 91(24):6269–6271, 1987.